Check for updates

Danming Wei[1]
Next Generation Systems Laboratory,
Louisville Automation and Robotics
Research Institute,
University of Louisville,
Louisville, KY 40208
e-mail: danming.wei@louisville.edu

Mariah B. Hall
Next Generation Systems Laboratory,
Louisville Automation and Robotics
Research Institute,
University of Louisville,
Louisville, KY 40208
e-mail: mariah.hall@louisville.edu

Andriy Sherehiy
Next Generation Systems Laboratory,
Louisville Automation and Robotics
Research Institute,
University of Louisville,
Louisville, KY 40208
e-mail: andriy.sherehiy@louisville.edu

Dan O. Popa
Next Generation Systems Laboratory,
Louisville Automation and Robotics
Research Institute,
University of Louisville,
Louisville, KY 40208
e-mail: dan.popa@louisville.edu

Design and Evaluation of Human–Machine Interface for NEXUS: A Custom Microassembly System

Microassembly systems utilizing precision robotics have long been used for realizing three-dimensional microstructures such as microsystems and microrobots. Prior to assembly, microscale components are fabricated using micro-electromechanical-system (MEMS) technology. The microassembly system then directs a microgripper through a series of automated or human-controlled pick-and-place operations. In this paper, we describe a novel custom microassembly system, named NEXUS, that can be used to prototype MEMS microrobots. The NEXUS integrates multi-degrees-of-freedom (DOF) precision positioners, microscope computer vision, and microscale process tools such as a microgripper and vacuum tip. A semi-autonomous human–machine interface (HMI) was programmed to allow the operator to interact with the microassembly system. The NEXUS human–machine interface includes multiple functions, such as positioning, target detection, visual servoing, and inspection. The microassembly system's HMI was used by operators to assemble various three-dimensional microrobots such as the Solarpede, a novel light-powered stick-and-slip mobile microcrawler. Experimental results are reported in this paper to evaluate the system's semi-autonomous capabilities in terms of assembly rate and yield and compare them to purely teleoperated assembly performance. Results show that the semi-automated capabilities of the microassembly system's HMI offer a more consistent assembly rate of microrobot components and are less reliant on the operator's experience and skill. [DOI: 10.1115/1.4049667]

Keywords: human–machine interface, semi-automated microassembly

1 Introduction

In the last three decades, robotic microassembly technology has been extensively investigated in a variety of applications of micro-electromechanical system (MEMS) devices [1–3]. Previously, researchers assembled micromechanical components and manipulated biological cells through manual operations [4]. However, there is an increasing demand for more complex and versatile microsystems comprising various materials like Si or GaAs as well as various metals, glass, and plastics that will require equally complex assembly [5]. Whenever larger volumes, smaller parts, higher precision, and/or extreme cleanliness are essential to fabrication requirements, robotic work cells are necessary to provide capabilities beyond human manual dexterity [6]. To facilitate an interaction between a human user and robotic work cells, researchers have proposed various human–machine interfaces (HMI), especially for semi-automated production [7]. In such production systems, humans can teleoperate robotic components and adjust the overall machine using feedback from sensors such as real-time vision. A multifunctional HMI for operating a microassembly system can improve the yield of the assembled products and the efficiency of the assembly process. Estevez [8] presented a haptic teleoperated microassembly system, which can provide force feedback to human users to achieve superior performance. Probst [2,3] and Popa [9,10] investigated a full six degrees-of-freedom (DOFs) microassembly system for manufacturing hybrid robotic MEMS devices.

In this paper, we present the NEXUS, a 9DOF microassembly system with a multifunctional human–machine interface integrating inverse kinematics, target inspection, and visual servoing to realize semi-automated assembly for microrobots. This HMI allows an operator to define and control tasks in the Cartesian workspace and achieve MEMS assembly with the help of two manipulators. An assembly process of Solarpede [11], a MEMS microrobot, was chosen to demonstrate NEXUS system HMI capabilities. In general, fully automated microassembly is very challenging, due to illumination conditions, MEMS component fabrication uncertainties, environmental conditions such as humidity and surface conditions. On the other hand, manual assembly through teleoperation by human operators is also very challenging and time-consuming due to a large number of variables such as positions in three-dimensional (3D) space, situational awareness from microscope cameras, and so on. The role of a semi-automated HMI is to automate certain parts of the assembly process while letting the operator perform other tasks through teleoperation. In this paper, we demonstrate that our proposed HMI scheme can greatly improve the operator's assembly rate for Solarpede microrobotic components.

This paper is organized as follows: in Sec. 2, we describe the NEXUS microassembly system as well as its underlying components and detail the Solarpede design and operational principles; in Sec. 3, we discuss the human–machine interface design for the NEXUS microassembly system and demonstrate how to assemble Solarpede using HMI to realize the semi-automation function; in Sec. 4, the experimental results are presented, including flexibility and functionality of the NEXUS microassembly system; finally, in Sec. 5, we conclude the paper and discuss future work.

2 Design of Microassembly System and Assembly Demonstrator

2.1 Nexus Microassembly System. The NEXUS microassembly system, shown in Fig. 1, was designed as a tool for semi-

[1]Corresponding author.

Contributed by the Manufacturing Engineering Division of ASME for publication in the Journal of Micro- and Nano-Manufacturing. Manuscript received July 15, 2020; final manuscript received December 31, 2020; published online February 1, 2021. Assoc. Editor: Ping Guo.

Downloaded from http://asmedigitalcollection.asme.org/micronanomanufacturing/article-pdf/8/4/041011/6627640/jmnm_008_04_041011.pdf by a0sher02@louisville.edu on 15 March 2021

automated assembly of three-dimensional MEMS-based structures and microrobots. It currently consists of two motional manipulators, M1 and M2, and an imaging system consisting of three lenses and cameras to monitor the process during microrobot assembly.

(1) Manipulator 1 (M1): it is a carrier manipulator that has a sample chuck as the end-effector to hold the sample die. The X and Y-axis manipulations are achieved by two motorized stages Newport® ILS250CC and Newport 433 series with LTA-HS, respectively. The rotational manipulation is performed by a motorized rotation stage Newport URS75BPP. Integration of three motorized stages results in M1 having 3 DOFs.
(2) Manipulator 2 (M2): it is a precise manipulator with a motorized *X-Y-Z* stage (Newport VP-25XA-XYZR) and a motorized rotation stage (Newport PR50CC), as well as a small manual translation stage. This combination of stages provides 6 (4 plus 2) DOFs. An end-effector with a microjammer or microgripper is mounted to the manual *X-Y* translation stage by the kinematic base (Newport BK-1A).
(3) The imaging system: a top camera (Edmund® EO-3112C) is attached to QIOPTIQ Optem® zoom tube lens combined with stepper motor controller; a side camera (Edmund EO-0413M) is attached to Edmund VZM450 zoom imaging lens; a back camera (Edmund EO-1312C) is attached to Edmund VZM 100i zoom imaging lens. These three cameras with zoom lenses are used to monitor the assembly process and provide real-time feedback on assembly status. Also, there are three illuminators providing light sources for the imaging systems.

In our previous study [12], we have investigated six different modular robotic kinematic configurations for effects on the yield of peg-in-hole assembly processes. The kinematic configurations contained five prismatic and revolute modular actuators, configured into 2MDOF configurations. Based on nominal precision errors for each actuator, the mechanisms were analyzed based on end-effector positioning errors during a peg-in-hole assembly task with given part tolerance limits. According to the yield results, the best mechanism geometries included rotation stages positioned at the distal end of the kinematic chains, for example, $XYZ\theta\phi$/Null or $XY\theta$/Zϕ, where X, Y, and Z are translations and θ and ϕ are rotations. The current NEXUS microassembly system follows a similar design philosophy and terminates manipulator kinematic chains with rotation degrees-of-freedom. The two kinematic chains in Fig. 1 contain stacked stages in arrangements $XY\phi$ (M1) and $XYZ\theta$ (M2), while the last two manual translation stages in M2 are simply used to calibrate the rotation centering position of the end-effector tip.

The combined precision of manipulator M1 and M2 is ± 5 μm in translation and ± 25 mdeg in rotation. The kinematic arrangement of these manipulators will aim to minimize rotation errors by placing a terminating roll joint after stacked translation stages. Because MEMS components fabricated on a silicon wafer are $2\frac{1}{2}$—dimensional, a combined 7DOF of relative spatial orientation, achieved by the NEXUS kinematic arrangement is sufficient for their microassembly. The microassembly will be realized with the help of a "jammer" microgripper located at the end of the M2 kinematic chain.

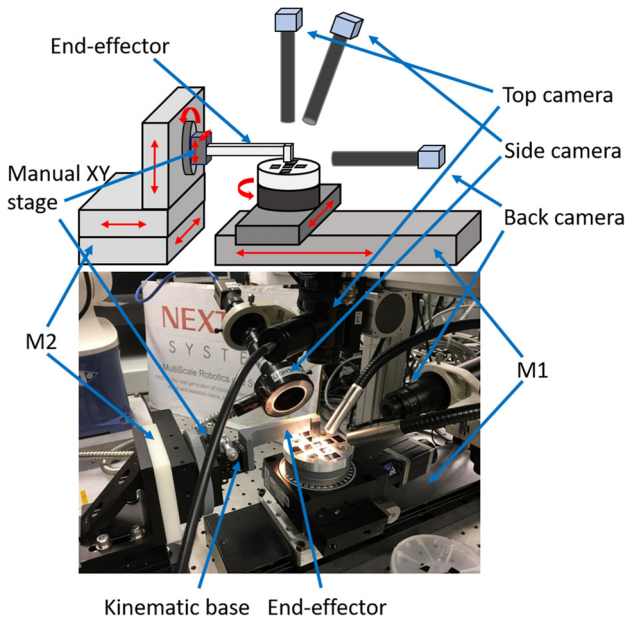

Fig. 1 NEXUS microassembly system schematic diagram and hardware setup

2.2 Solarpede Microrobot. Solarpede is a novel untethered MEMS microrobot powered by solar cells whose principle of motion is based on the stick-and-slip mechanism. Solarpede is intended to operate as a part of microfactories where it could be a conveyor or transportation system. Solarpede's body consists of the "backpack"—containing solar cells, control circuitry, and motion module—die with MEMS structures. The Solarpede's die consists of eight in-plane chevron electrothermal actuators and eight vertical legs which were fabricated on a silicon-on-insulator wafer by using silicon-on-insulator deep reactive ion etching (DRIE) processes with 100 μm thickness device layer [13,14]. Solarpede's components are presented to the microassembly system as centimeter-size die cut from the fabricated wafer.

There are two types of leg arrangements on Solarpede's die body as shown in Fig. 2: a diagonal leg arrangement (on the left) allows the motion of Solarpede in an omni-direction while the parallel leg arrangement (on the right) results in nonholonomic motion of the Solarpede.

Solarpede's MEMS legs were assembled perpendicular to the body (e.g., the die) where they were attached to electrothermal actuator sockets with the help of the Zyvex snap-fastener structures and ultraviolet (UV) curable adhesive [15]. Figure 3 depicts the dimension of a single leg and socket along with a chevron actuator and jammer which was mounted on the end-effector of M1 to pick-and-place the Solarpede's legs. Thus, each microrobot contains eight 100 μm-thick legs, and their compliant placements into Zyvex sockets required 5 μm positional precision for the assembly to succeed with high yield.

3 Human–Machine Interface Description

The NEXUS human–machine interface, as shown in Fig. 4, was developed using National Instruments (NI; Austin, TX) LabVIEW® and NI Vision Assistant module for the NEXUS microassembly system. NI Vision Assistant is capable of a variety of tasks such as vision acquisition, image processing, and target

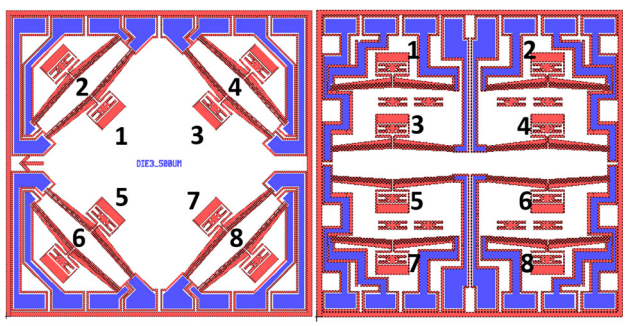

Fig. 2 Solarpede body L-edit layout design: omnidirectional motion (left) and nonholonomic directional motion (right)

Downloaded from http://asmedigitalcollection.asme.org/micronanomanufacturing/article-pdf/8/4/041011/6627640/jmnm_008_04_041011.pdf by a0sher02@louisville.edu on 15 March 2021

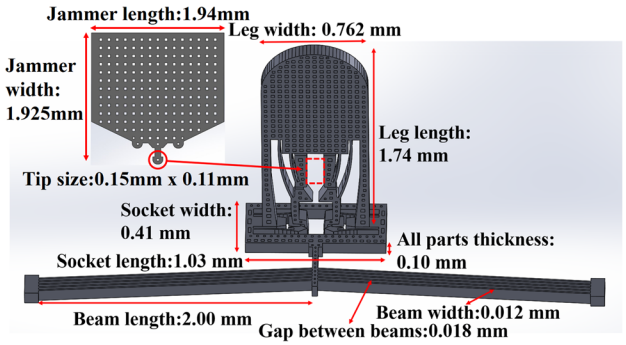

Fig. 3 The dimension of a single leg assembled into the chevron actuator and the jammer

tracking. As a part of the HMI, those functions allow tracking of specific targets (based on the defined templates) with the help of visual feedback from cameras. The HMI utilizes inverse kinematic functions to assist with coarse adjustment and manipulation of the target. It also includes an inspection module to filter out viable assembly targets by checking each component to be assembled (e.g., Solarpede's legs), before trying to pick and place them into the desired sockets. The integrated visual servoing module can assist operators to make fine adjustments to the targets to achieve the desired configuration. Otherwise, it includes a semi-automated function to sequence the assembly operations and complete the assembly of Solarpede microrobots.

The individual modules of the NEXUS HMI are further described in the Secs. 3.1–3.3.

3.1 Positioning Module. In the positioning module, the inverse kinematic function is applied to provide a convenient and reliable operation for the operator. This allows the operator to manipulate the target by sending Cartesian part position and orientation commands, and then the interface will calculate appropriate joint commands for the M1 and M2 robots.

One example of the use of automated inverse kinematics is after the system's initialization, the operator tries to move the desired assembly target into the field of view (FOV) of the top camera. To

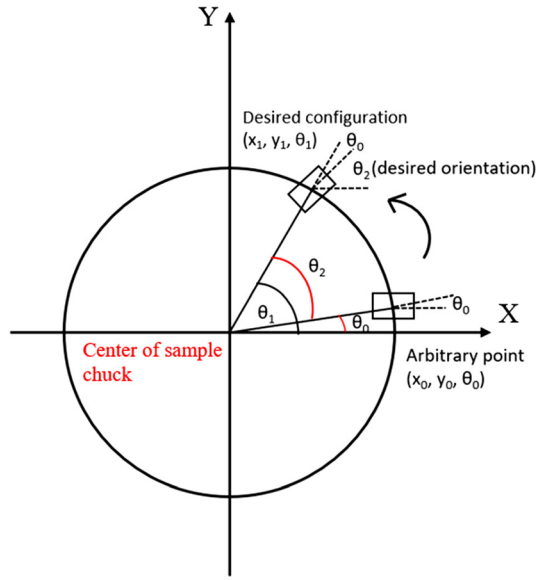

Fig. 5 An arbitrary point moves to the desired configuration by inverse kinematic function

initialize the system, the center of the chuck on M1 is matched to the center of the FOV of the top camera. It is recorded as the base frame coordinate (0, 0, 0) representing the linear X-axis, Y-axis, and the rotation θ-axis, respectively. Let (x_0, y_0, θ_0) represents an arbitrary point of the desired target on the chuck as shown in Fig. 5, then if the target is supposed to rotate the desired orientation θ_2, the target will be moved to a new position (x_1, y_1, θ_1), where $\theta_1 = \theta_0 + \theta_2$. Now if need to center this point with respect to the top camera, the linear stages will be displaced linearly by $-x_1$ and $-y_1$ in X and Y directions, respectively. Note that in this case, the orientation of the sample chuck mounted on M1 will still be maintained at θ_1.

The mathematic relationship between the arbitrary point and its desired configuration is shown in the following equations:

$$\theta_0 = \tan^{-1}\left({}^{y_0}/_{x_0}\right) \tag{1}$$

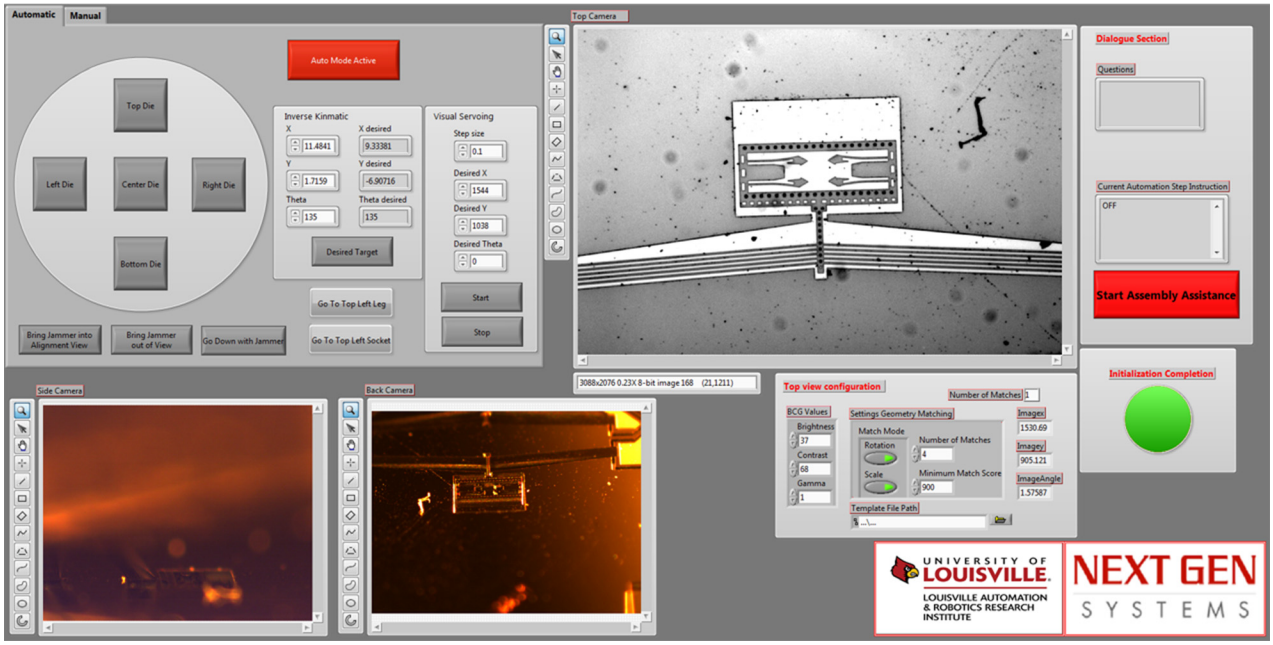

Fig. 4 The entire human–machine interface of the NEXUS microassembly system

Downloaded from http://asmedigitalcollection.asme.org/micronanomanufacturing/article-pdf/8/4/041011/6627640/jmnm_008_04_041011.pdf by a0sher02@louisville.edu on 15 March 2021

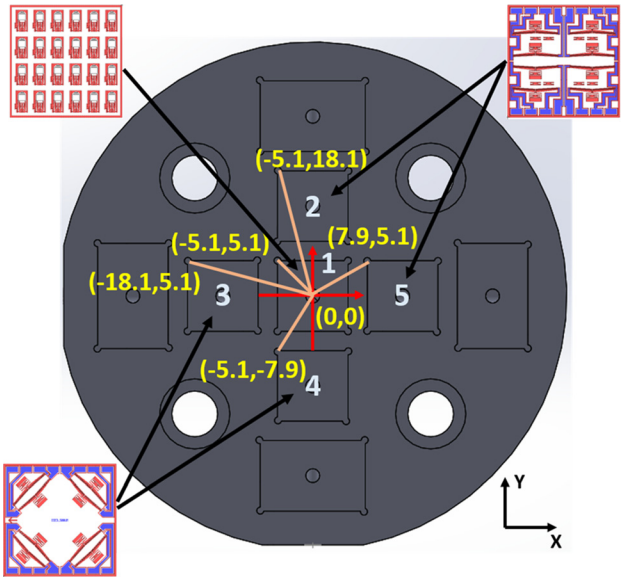

Fig. 6 Die distribution and coordinates of top-left corner referred to the origin on the sample chuck

$$\theta_1 = \theta_0 + \theta_2 \tag{2}$$

$$x_1 = \sqrt{x_0{}^2 + y_0{}^2}\cos\theta_1 \tag{3}$$

$$y_1 = \sqrt{x_0{}^2 + y_0{}^2}\sin\theta_1 \tag{4}$$

The repeatability of the M1 stages has been experimentally evaluated in Sec. 4.3. We are summarizing it in this section with quantitative information. Using the above equations, any arbitrary points on the chuck can be moved into the FOV of the top camera, since the repeatability of M1 stages is below 10 μm, while the FOV is 1.08 mm^2 that is projected onto a pixel area of 3088 × 2076 at 7× magnification of the top view.

In order to determine the initial coordinates x_0 and y_0 of an arbitrary point of an assembly target, two different coordinate systems are used, namely, the chuck coordinate system and the individual die layout coordinate system. For example, Fig. 6 shows the top-left corner coordinates of each die in the chuck coordinate system where the origin is at the center of sample chuck and, coincidentally, die#1.

After loading the die samples on the sample chuck, such as the distribution of dies shown in Fig. 6, the assembly target point coordinate must be measured in the die layout coordinate system for transferring to the chuck coordinate system. Figure 7 indicates that 12 random points of targets were selected from three different dies and their coordinates referred to the top-left corner of each die. Table 1 shows each random point coordinate referred to the origin of the sample chuck after calculation.

In this manner, the inverse kinematics procedure can be started when the coordinate of any target's point in the chuck coordinate system entered into NEXUS microassembly system HMI, and then the target can be centered in the FOV of the top camera. Naturally, additional configuration errors have to be considered during this operation, which will be discussed in Sec. 4.

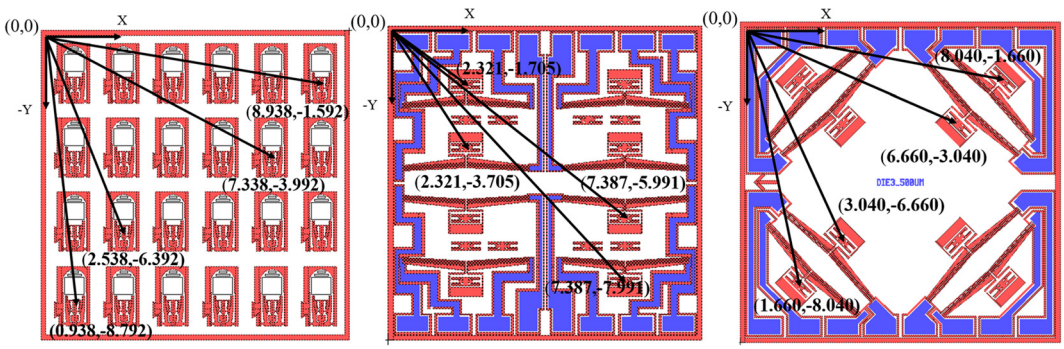

Fig. 7 The center of legs and sockets coordinates referred to the top-left corner

Table 1 Randomly selected points of target coordinates of die samples

		Coordinates in the die layout coordinate system (mm)		Coordinates in the sample chuck coordinate system (mm)	
	No. of points	*X*	*Y*	*X*	*Y*
Die#1 with legs	1	8.938	−1.592	3.838	3.508
	2	7.338	−3.992	2.238	1.108
	3	2.538	−6.392	−2.562	−1.292
	4	0.938	−8.792	−4.162	−3.692
Die#2 with parallel sockets	1	2.321	−1.705	−2.779	16.395
	2	2.321	−3.705	−2.779	14.395
	3	7.387	−5.991	2.287	12.109
	4	7.387	−7.991	2.287	10.109
Die#3 with diagonal sockets	1	8.040	−1.660	−10.060	3.440
	2	6.660	−3.040	−11.440	2.060
	3	1.660	−8.040	−16.440	−2.940
	4	3.040	−6.660	−15.060	−1.560

Downloaded from http://asmedigitalcollection.asme.org/micronanomanufacturing/article-pdf/8/4/041011/6627640/jmnm_008_04_041011.pdf by a0sher02@louisville.edu on 15 March 2021

3.2 Target Detection. Due to the nature of the MEMS fabrication process, MEMS structures will contain dimensional tolerances within a few micrometers. Target evaluation detection, e.g., estimation of assembly location, has been implemented on the NEXUS human–machine interface. In the case of the Solarpede's leg die, the operator needs to evaluate the structure for physical integrity using visual feedback. Then, each microrobot leg that awaits assembly is detected by the interface based on an imported template from the structure's CAD file. During the leg detection, when one leg is brought into the FOV of the top camera, a question "Do you want to use this snap fastener?" appears in the dialog section in the HMI, the operator can decide whether the leg will be pick up or not by clicking "Yes" or "No" button. If the leg is not viable, for instance, if it is damaged during fabrication, the operator just clicks the "No" button, then the M1 will bring the next leg to the FOV of the top camera for checking its viability. This process repeats until finding the viable leg on a given die.

The sequence of the target detection on the Solarpede's leg die was programmed by default starting from the top-left corner, moving right, and then moving to the second line from left to right, repeating the scanning steps until detecting the bottom-right corner at the bottom line. However, since there are two different geometric arrangements for the sockets shown in Fig. 2, the interface was also programmed to follow the socket numbers on the parallel and diagonal arrangements from 1 to 8 to check each socket viability. Similarly, the sequence of leg assembly steps also follows the same numbers on each substrate.

3.3 Visual Servoing. After the desired target has been selected for the assembly, a fine adjustment of the end-effector and target positioning becomes an indispensable step in the process. This step is performed using visual servoing, which is based on real-time image signal as feedback to the operator to actuate multiple motorized stages to do fine adjustment for a specific feature as a template to move to the desired position.

Visual servoing as a calibration method based on visual feedback for closed-loop control has been employed to enhance the accuracy and flexibilities of the robot system [16–18]. Following the classic visual servoing theory, applied to a microscope and fine position adjustment of microparts, we employ image Jacobian. Servoing using the image Jacobian from microscope images is a popular visual tracking technique ideally suited to the micro- and nanoscale [19]. In contrast to other visual tracking schemes, such as position-based servoing, this method does not estimate positions in global Cartesian frames from images, which can be prone to measurement errors. With the help of image Jacobian, we can determine the path which the target follows to move to the desired position by steps based on the target current position. The differences of target center configuration in the top image coordinate in pixels have a relationship with image Jacobian and the configuration of target center differences shown in Eq. 5. Furthermore, the image Jacobian J_{image} is a 3×3 matrix and can be expressed in Eq. (6) as shown below:

$$\begin{bmatrix} \Delta P_x \\ \Delta P_y \\ \Delta p_\theta \end{bmatrix} = J_{\text{image}} \begin{bmatrix} \Delta X \\ \Delta Y \\ \Delta \theta \end{bmatrix} \tag{5}$$

$$J_{\text{image}} = \begin{bmatrix} J_{11} & J_{12} & J_{13} \\ J_{21} & J_{22} & J_{23} \\ J_{31} & J_{32} & J_{33} \end{bmatrix} \tag{6}$$

where ΔX, ΔY, and $\Delta\theta$ are the variations of the X, Y, and rotation stages in M1; ΔP_x, ΔP_y, and ΔP_θ are variable pixel values of the template in the FOV of the top camera. The nine values of image Jacobian entries can be calculated by calibration from a set of at least three features with known dimensions on the target die [10,20].

After acquiring the image Jacobian, the target motions to the desired position with the desired orientation can be planned with the following equation:

$$\begin{bmatrix} X_{\text{new}} - X_C \\ Y_{\text{new}} - Y_C \\ \theta_{\text{new}} - \theta_C \end{bmatrix} = \Delta s J_{\text{image}}{}^{-1} \begin{bmatrix} P_{X_d} - P_{X_c} \\ P_{Y_d} - P_{Y_c} \\ P_{\theta_d} - P_{\theta_C} \end{bmatrix} \tag{7}$$

where X_C, Y_C, θ_C, X_{new}, Y_{new}, and θ_{new} are the current and new positions of X, Y, rotation stage of M1, respectively. P_{Xd}, P_{Yd}, $P_{\theta d}$, P_{Xc}, P_{Yc}, and $P_{\theta c}$ are pixel values of the desired and current pose of the assembly template in the FOV of the top camera. Δs is defined as the step size of movement of the M1 stages. Combining inverse kinematic and visual servoing functions of M1, the microstructure can be moved to the desired configuration with more precision and reliability. Those provide a trusted basement for assembling legs in a three-dimensional structure.

3.4 Semi-Automated Assembly. In this section, we describe how an operator assembles Solarpede legs using the NEXUS-HMI with semi-automated function following Solarpede's leg assembly flow as shown in Fig. 8. First, the operator loads dies with the fabricated leg and sockets/actuators on the chuck of M1 (see in Fig. 6). Then, the operator can select leg die to move to the FOV of the top camera and then inspect the legs one by one until finding the good quality leg; next, once the leg is selected, it will be moved to the desired position with the desired orientation by using visual servoing function with the leg template and ready to be picked up. Then, the jammer mounted on the end-effector of M2 is moved into the FOV of the cameras. The operator controls the jammer to break a tether holding the leg in-plane on a die. The operator will need to align the jammer tip and pick up the leg by inserting it into the top gripper of the snap-fastener structure. Once the leg is picked up and then rotated by 90 deg, the operator can deposit a pool of UV curable epoxy on the chuck and dip the bottom sides of the leg in it. After the epoxy has been carefully attached to the leg, the jammer with the leg is moved out of the FOV of the top camera, then the socket die is brought into the view. Each socket is inspected until finding a good socket. At this time, the socket template is used to align the socket by visual servoing function; finally, the operator controls M2 to bring the leg back to the top view and place it into the socket to complete the leg assembly. Zyvex snap-fastener's lock mechanism allows the leg to be secured in the socket. After the jammer is removed from the leg, UV light is applied to cure the UV epoxy which would ensure the leg's secure attachment to the actuator's socket. Thus, the whole leg assembly process combines both manual and automated operations, where some operations have to be completed

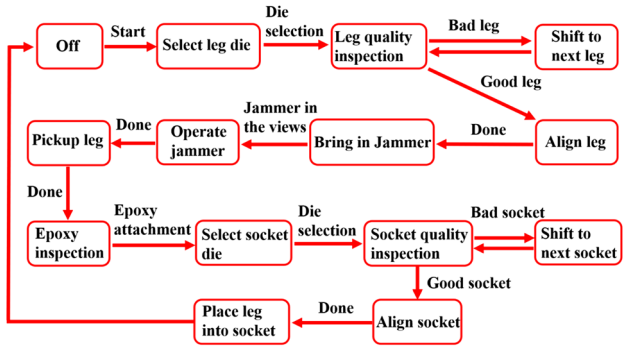

Fig. 8 Block diagram of Solarpede leg assembly flow using the NEXUS-HMI

Downloaded from http://asmedigitalcollection.asme.org/micronanomanufacturing/article-pdf/8/4/041011/6627640/jmnm_008_04_041011.pdf by a0sher02@louisville.edu on 15 March 2021

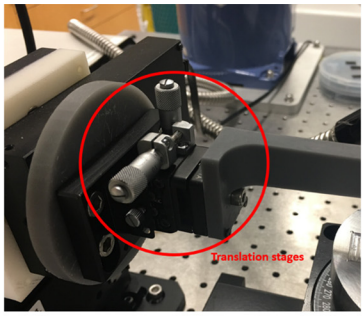

(*a*)

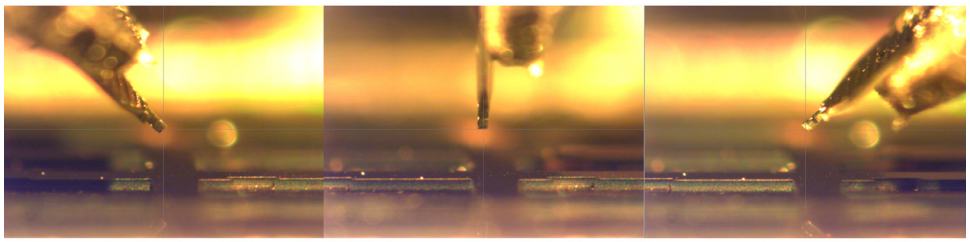

(*b*)

Fig. 9 (*a*) Translation stages on M2 and (*b*) rotation centering of microjammer tip

Table 2 Configuration errors of randomly selected points which are supposed to the FOV center of the top camera

	No. of sockets or legs	X (μm)	Y (μm)	θ (deg)
Die#3 diagonal sockets	3	344.97	−65.92	0.69
	4	335.76	−65.35	0.69
	5	367.92	−57.25	0.70
	6	377.80	−52.29	0.70
	Average	356.61	−60.20	0.695
	Standard deviation	16.93	3.60	0.01
Die#4 diagonal sockets	3	414.05	107.60	0.57
	4	417.60	107.21	0.55
	5	431.31	108.62	0.42
	6	424.38	107.62	0.58
	Average	421.84	107.76	0.53
	Standard deviation	6.61	0.52	0.06
Die#2 parallel sockets	1	199.09	204.18	1.03
	3	225.67	203.29	1.03
	6	272.55	143.61	1.07
	8	304.01	147.13	1.03
	Avg.	250.33	174.55	1.04
	Standard deviation	40.65	29.21	0.02
Die#5 parallel sockets	1	410.08	272.71	0.61
	3	423.97	271.14	0.62
	6	446.76	236.17	0.68
	8	467.52	239.52	0.64
	Average	437.08	254.89	0.64
	Standard deviation	21.92	17.09	0.03
Die#1 legs	6	180.93	284.38	0.82
	11	186.21	287.31	0.78
	14	199.58	301.24	0.73
	19	213.13	307.00	0.78
	Average	194.96	293.48	0.78
	Standard deviation	12.50	9.42	0.03

manually, while others can be automatically executed using the NI LabVIEW program.

4 Results and Discussion

4.1 Nexus Calibration. The calibration of the NEXUS microassembly system is necessary before conducting successful experiments. First, the three microscope cameras employed in the imaging system were aligned for focusing on the same area from three different view directions (top, side, and back views). Second, a rotation centering technique was employed for calibration of microjammer end-effector mounted on M2 and used for picking and placing the Solarpede legs. In this step, the small manual X-Y translation stage, in Fig. 9(*a*), was adjusted so that the

Downloaded from http://asmedigitalcollection.asme.org/micronanomanufacturing/article-pdf/8/4/041011/6627640/jmnm_008_04_041011.pdf by a0sher02@louisville.edu on 15 March 2021

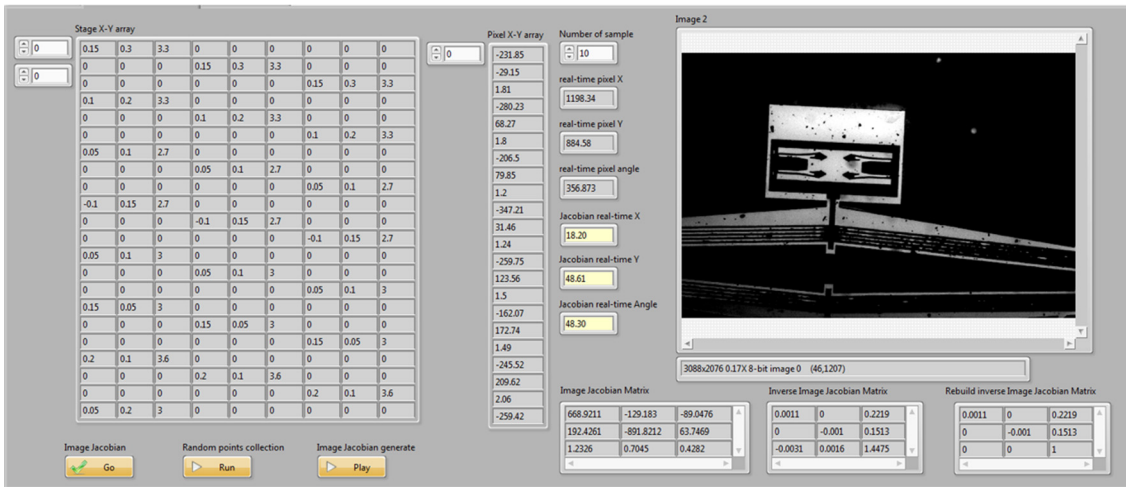

Fig. 10 The interface for generating image Jacobian

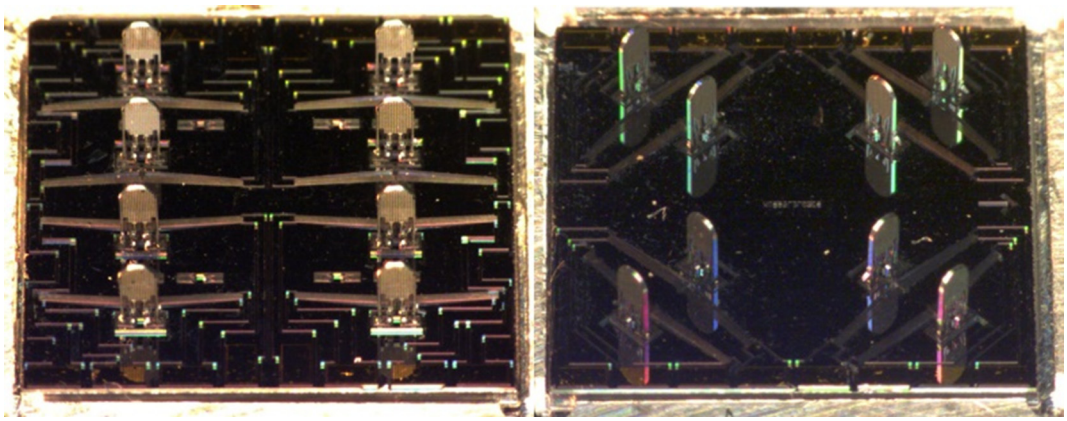

Fig. 11 Actual Solarpede bodies with eight assembled legs in parallel (left) and diagonal (right) socket arrangements

microjammer tip reaches the kinematic center of the rotation stage. During the end-effector rotation, the tip of the microjammer can be maintained at one point as shown in Fig. 9(*b*). In this manner, the micropart picked up by the microjammer can always appear in the FOV of the side view when the microjammer rotates, which can help the operator monitor the motion of the micropart to avoid crash and damage during the motion.

Third, to calibrate the inverse kinematic functions of M1, we randomly selected 20 points from leg and socket dies following the die distribution in Fig. 6. The number of sockets follows the Solarpede body die in Fig. 2, the number of legs is counted from left to right and from top to bottom in the leg die, totaling 24 legs. Table 2 presents the configuration errors which occur when the targets (legs and sockets) are supposed to move to the FOV center of the top camera. The measured values received from the images are in pixel, after calculated with 7× magnification of the top view, the ratio between pixel and μm is 1:0.644. From Table 2, the configuration errors of each die are different because when loading dies on the chuck, each die has a different initial configuration. However, in the same die, each point has nearly constant configuration errors. Also, those configuration errors are acceptable for the NEXUS system because the goal is to use the inverse kinematic function to move any arbitrary targets on the chuck into the FOV of the top camera and be ready for the visual servoing operation.

Fourth, before doing the visual servoing operation, an image Jacobian matrix will be generated by collecting the configuration data of the target template which is randomly moving to different positions (e.g., 10 positions). If the magnification of the top camera lenses is fixed, the image Jacobian matrix will be constant. Based on Eqs. (5) and (6), image Jacobian J_{image} will be calculated, then inverse image Jacobian J_{image}^{-1} is used in Eq. (7). Δs step size determines the target moving distance from an arbitrary point to the desired point. A specific LabVIEW programming interface for generating image Jacobian was created as shown in Fig. 10. By using this interface, the target template can automatically move to different points randomly based on the number of points input. Meanwhile, the configuration of the target template can be recorded while moving to each point. All the recorded data are for the calculation of image Jacobian and inverse image Jacobian. Inverse image Jacobian in Eq. (8) was created using the LabVIEW program and applied to Eq. (7) for the visual servoing function in the NEXUS HMI

$$J_{\text{image}}^{-1} = \begin{pmatrix} 0.0011 & -0.0001 & -0.1252 \\ 0 & -0.001 & 0.1633 \\ 0.0001 & 0.0002 & 1.0052 \end{pmatrix} \tag{8}$$

Finally, after calibration, the proper assembly sequence of Solarpede's leg assembly should be considered during operation to avoid possible part collisions with the end-effector. For the Solarpede with the parallel arrangement of sockets, the assembly sequence is straightforward in order of the assigned socket

Downloaded from http://asmedigitalcollection.asme.org/micronanomanufacturing/article-pdf/8/4/041011/6627640/jmnm_008_04_041011.pdf by a0sher02@louisville.edu on 15 March 2021

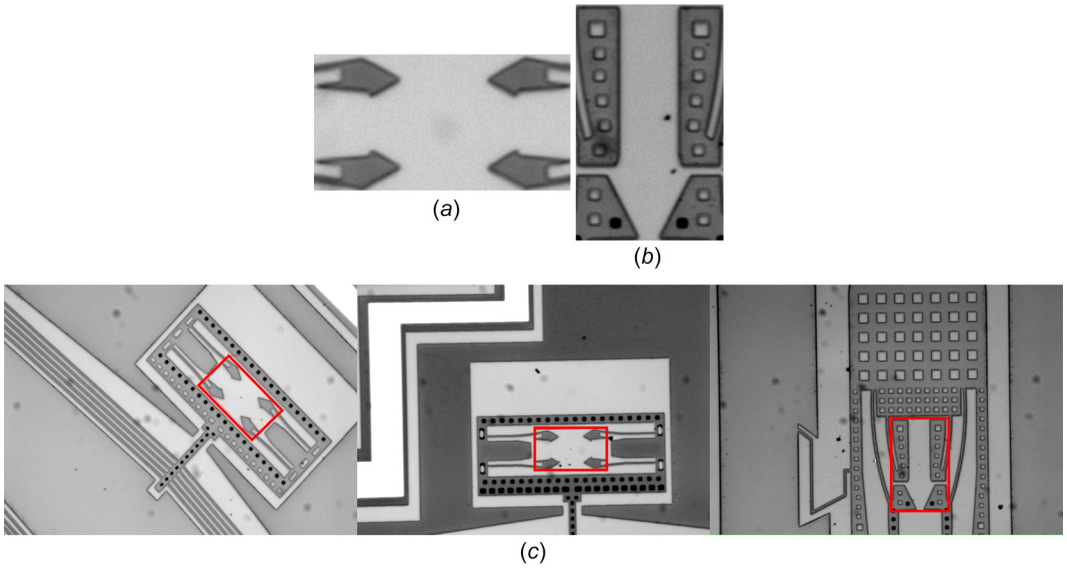

Fig. 12 (*a*) and (*b*) are the templates for socket and leg, respectively; (*c*) presents the targets with templates moving to FOV of the top camera with the inverse kinematic function

numbers– from 1 to 8 (see Fig. 2). However, for the Solarpede diagonal socket arrangement, there are at least two assembly options: (1) first four legs are placed into the 4 inner sockets (like following 1, 3, 5, and 7), and then, the next four legs are placed into the four outer sockets (like following 2, 4, 6, and 8); (2) for each corner, the leg is assembled first on the inner socket, followed by the outer socket (like following 1–2, 3–4, 5–6, and 7–8). Figure 11 displays Solarpede dies with successfully assembled legs for both parallel and diagonal socket arrangements.

4.2 Template Generation in Human–Machine Interface. In the NEXUS HMI, the templates are generated before initiation of the calibration procedure and use of the visual servoing. With the NI Vision Assistant, a proper template can be generated after a series of digital imaging processes, like adjusting contrast, brightness, and gamma parameters, and performing color extraction and pattern matching. Those steps are critical for the target recognition by the Vision Assistant. Figure 12 depicts the generated templates (a is for the socket, and b is for the leg) which are the processed images of the specific structures of the targets. When the assembly target (socket or leg) is moved to the FOV of the top camera by the positioning module with inverse kinematic function, the template can be recognized using the LabVIEW program automatically. It has to be noted that during this process, configuration errors are always present, so fine calibration has to be done with visual servoing. Template generation is particularly important in the further development of the full automation of the picking up and placing tasks for the microstructure. It is significantly useful for the visual servoing to move the target to the desired position for picking up and placing.

4.3 Evaluation of the NEXUS System Human–Machine Interface. Before conducting experiments, we evaluated the repeatability of manipulators M1 and M2 of the NEXUS microassembly system. The top and side cameras were setup at 7× and 4× magnifications, respectively, resulting in an accuracy of 0.41 μm/pixel for the top view and an accuracy of 0.7 μm/pixel for the side view to obtain the acceptable target templates for the image processing. The top view was used to measure *X*-*Y* translation and rotation repeatability of M1 and *X*-*Y* of M2, the side view was applied to measure Y-Z translation and rotation repeatability of M2. To measure the repeatability of M1, a socket template with a certain orientation on the sample chuck was selected, the

Table 3 The measured repeatability of M1 and M2

	M1 measured repeatability	M2 measured repeatability
X (μm)	8.17	5.29
Y (μm)	3.37	3.59
Z (μm)	N/A	1.68
θ (mdeg)	28	21

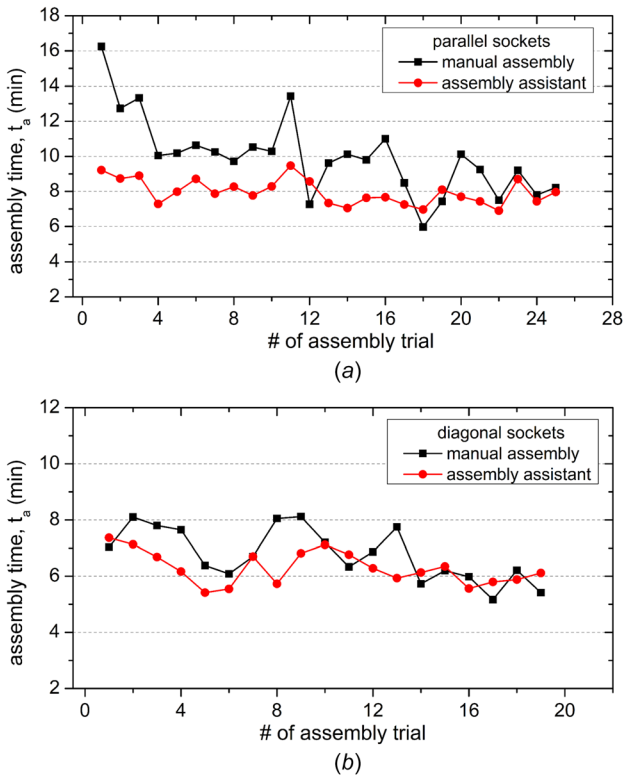

Fig. 13 Comparison of leg assembly time duration for manual and semi-automated operations in case of the: (*a*) parallel socket arrangement and (*b*) diagonal socket arrangement of the Solarpede

Downloaded from http://asmedigitalcollection.asme.org/micronanomanufacturing/article-pdf/8/4/041011/6627640/jmnm_008_04_041011.pdf by a0sher02@louisville.edu on 15 March 2021

Table 4 Statistical analysis of the assembly time variation of manual and semi-automated modes for two different socket arrangements

Socket arrangement	Parallel		Diagonal	
Mode	Manual	Semi-automated	Manual	Semi-automated
# of trials	25	25	19	19
Mean assembly time (min)	9.97	7.97	6.78	6.29
Standard deviation (min)	2.23	0.71	0.94	0.58
Variance (min)	4.98	0.51	0.88	0.34
Maximum time (min)	16.25	9.47	8.12	7.37
Minimum time (min)	5.97	6.90	5.17	5.42
Total time (Sum) (min)	249	199	129	120

coordinate of the center of the socket template and orientation referred to the stages was set as the end point. An arbitrary point on the sample chuck was selected as the starting point. The motions of forth and back between the starting point and the end point were completed in 25 trials. The coordinate of the center of the socket template was recorded when the center was brought back to the FOV of the top view in each trial for calculating the M1 repeatability. For the M2, the repeatability was measured on the center of the jammer tip template. Every 25 trials were done from the top view and side view via the same method for M1 repeatability measurement. The measured repeatability of M1 and M2 are depicted in Table 3.

In order to test the efficiency of the NEXUS-HMI with the semi-automated function, we have designed the experiment where a total of 88 legs (25–25 for parallel socket arrangement and 19–19 for diagonal socket arrangement) have been assembled using the NEXUS system in semi-automated mode (with the help of the HMI assembly assistant) and also in full manual mode (with Newport XPS controller graphical user interface). We have determined that for the parallel socket arrangement, semi-automated assembly was 16% more successful than the manual operation and overall faster. Figure 13 presents values of recorded time duration (t_a) of assembly of a single Solarpede's leg in both semi-automated and full manual modes. As it can be clearly seen in the case of the parallel socket arrangement assembly times of the semi-automated operation are smaller for a majority of the trials when compared to manual mode. This time difference is less pronounced for the diagonal socket arrangement. Nevertheless, if we compare the average assembly time, the total time of all trials combined for four cases (Table 4), the advantage of semi-automated mode is evident. For the parallel arrangement, it takes on average around 2 min faster to assemble the Solarpede's leg with the help of the assembly assistant, whereas in the case of the diagonal die, it is below 1 min. If we consider combined times of all the trials for the parallel and diagonal arrangement difference between two assembly modes amount up to 50 min (25 trials) and 9 min (19 trials), respectively (Table 4), in favor of the semi-automated assembly.

Another important factor that we have considered during the evaluation of our HMI assembly assistant is the consistency of the assembly process duration, determined by the variation of time from trial to trial. For the parallel socket arrangement, it is clearly visible (Fig. 13–a) that the time duration of assembly in the manual mode is decreasing with each trial (from 16 to 18 min), where it is comparable with semi-automated mode toward the end of the experiment—trials 22–25; in some case, it is even lower—trial 12, 18, and 19. It can be explained by the increased confidence of the NEXUS system operator during the manual mode with a larger number of trials. However, due to the user's fatigue and human error assembly time usually repeatedly increases. It is also

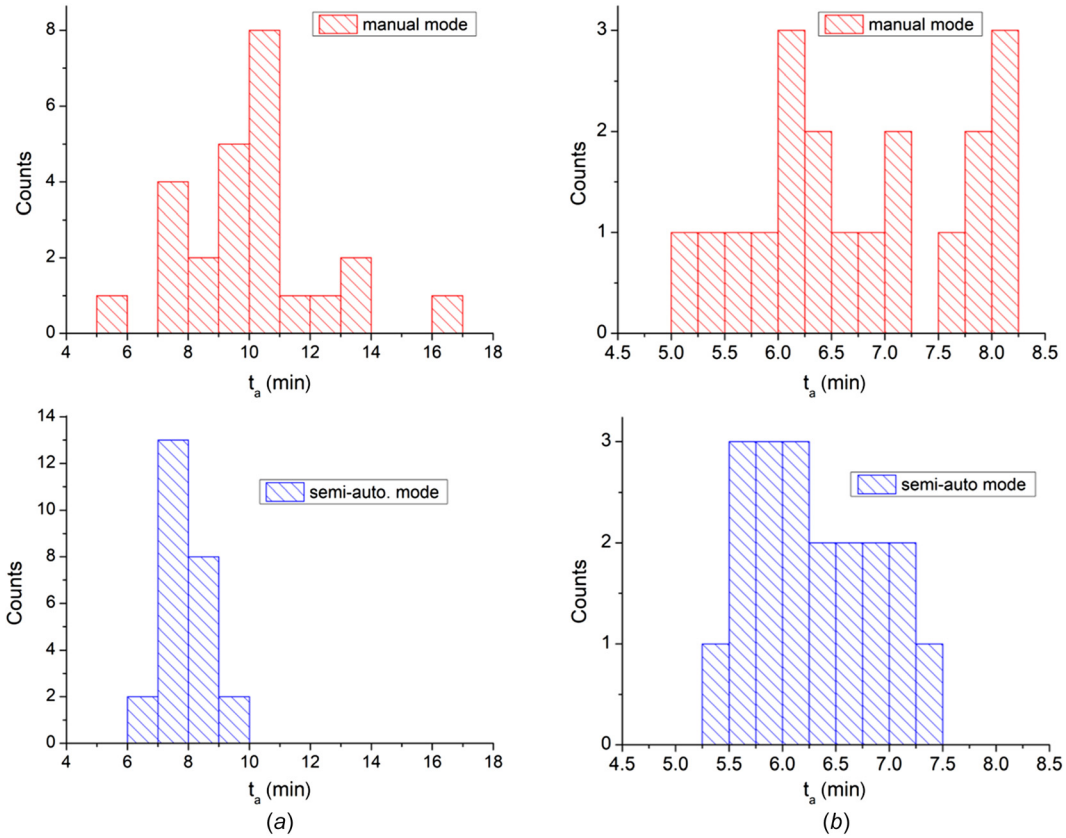

Fig. 14 Distribution of the assembly times, t_a for manual and semi-automated modes in case of the: (*a*) parallel socket arrangement and (*b*) diagonal socket arrangement

Downloaded from http://asmedigitalcollection.asme.org/micronanomanufacturing/article-pdf/8/4/041011/6627640/jmnm_008_04_041011.pdf by a0sher02@louisville.edu on 15 March 2021

indicated by fluctuations in time duration of assembly for the manual mode, which are more significant from trial to trial compared to the semi-automated mode for which we observe the more consistent result, where assembly duration is slightly fluctuating around 8 min for all 25 trials. A similar pattern can be observed for the diagonal die (Fig. 13(*b*)), where the duration of the manual operation is longer (in most of the cases) for the trials 1–13, and then from 14 trial to 19, it is comparable with t_a of semi-automated mode, However, the difference in assembly time fluctuation for the diagonal arrangement is a harder to notice based in Fig. 13(*b*). The analysis of the assembly time distribution for all four cases (Fig. 14) indicates that semi-automated operation t_a has significantly smaller variations from trial to trial as compared to the manual mode. Additional evidence to support this argument comes from the results of quantitative analysis experimental data, specifically assembly times. Values of the standard deviation and variance are lower for the semi-automated mode than in the case of the manual for both socket arrangements (Table 4). Those two quantities measure the spread of the trials' data relative to the mean value.

Interestingly, in the case of the diagonal arrangement, the difference between semi-automated and manual modes is not that significant as in the case of the parallel dies. We can speculate that it is related to the specificity of the manual assembly of the die with the diagonal socket arrangement, in which case it might be easier and more precise to determine coordinates of the microstructure's components, This is reflected by lower configuration errors as evidenced by the fact that values of the standard deviation in Table 2 are significantly smaller for dies of the diagonal socket arrangement compared to the ones of parallel socket arrangements.

5 Conclusion

In this paper, we introduce a multifunctional semi-automated human–machine interface for a custom flexible microassembly system. With inverse kinematic, target detection, and visual servoing functions realized with the help of NI LabVIEW. We have demonstrated that the semi-automated human–machine interface improves the assembly process of Solarpede microrobot by reducing time, increasing efficiency, and making it more consistent across trials and users. NEXUS microassembly system can be used for the assembly of the other various types of microrobots or microstructures introducing a corresponding modification to the human–machine interface. In general, the NEXUS HMI was created to assemble $2^1/_2$D MEMS components using the Zyvex jammer and socket snap fasteners. For this type of geometries, Solarpede is a very generic and illustrative microrobot. For other applications, for example, handing of non-silicon, transparent components, and 3D micromachined shapes, the HMI will need to be modified to help the operator improve situational awareness and reduce automation errors in other specific challenging assembly situations. For other microrobots, like sAFAM [21] and Chevbot [22] that we are investigating, other specific HMIs should be programmed using the NEXUS system because different microrobots have different specific structures, different assembly flow steps, and different tolerance of assembly. In the future, we will develop a more compatible HMI for multiple microrobot assembly. Ultimately presented in this paper, NEXUS HMI can be further developed and upgraded to reach fully automated assembly of the MEMS-based microrobots or microstructures, as well as a diverse tool for research on automation and control in the microrobots.

Acknowledgment

We would like to thank the staff of University of Louisville's Micro-Nano Technology Center (MNTC) for their great suggestion and help in fabricating Solarpede components.

Funding Data

- National Science Foundation (Grant No. MRI #1828355; Funder ID: 10.13039/100000001).
- National Science Foundation (Grant No. RII Track-1#1849213; Funder ID: 10.13039/100000001).

References

[1] Xie, H., Rong, W., Sun, L., and Chen, L., 2006, "A Flexible Microassembly System for Automated Fabrication of MEMS Sensors," Proceedings of Ninth International Conference on Control, Automation, Robotics and Vision, Singapore, Dec. 5–8, pp. 1–6.

[2] Probst, M., Hürzeler, C., Borer, R., and Nelson, B. J., 2009, "A Microassembly System for the Flexible Assembly of Hybrid Robotic Mems Devices," Int. J. Optomechatronics, **3**(2), pp. 69–90.

[3] Probst, M., Borer, R., and Nelson, B. J., 2007, "A Microassembly System for Manufacturing Hybrid Mems," Proceedings of the 12th IFToMM World Congress, IFToMM, Besancon, June 18–21.

[4] Huang, X., Lv, X., and Wang, M., 2006, "Development of a Robotic Microassembly System With Multi-Manipulator Cooperation," Proceedings of International Conference on Mechatronics and Automation, Luoyang, China, June 25–29, pp. 1197–1201.

[5] Cohn, M. B., Boehringer, K. F., Noworolski, J. M., Singh, A., Keller, C. G., Goldberg, K. A., and Howe, R. T., 1998, "Microassembly Technologies for MEMS," Proceedings of Microelectronic Structures and MEMS for Optical Processing IV, International Society for Optics and Photonics, Sept. 2, Vol. 3513, pp. 2–16.

[6] Hollis, R. L., and Rizzi, A. A., 2004, "Agile Assembly Architecture: A Platform Technology for Microassembly," Proceedings of American Society for Precision Engineering 19th Annual Meeting, Orlando, FL, Oct. 26–28.

[7] Langer, M., and Söffker, D., 2011, "Human Guidance and Supervision of a Manufacturing System for Semi-Automated Production," Proceedings IEEE Jordan Conference on Applied Electrical Engineering and Computing Technologies (AEECT), Jordan, Amman, Dec. 6–8, pp. 1–6.

[8] Estevez, P., Khan, S., Lambert, P., Porta, M., Polat, I., Scherer, C., Tichem, M., Staufer, U., Langen, H. H., and Schmidt, R. M., 2010, "A Haptic Tele-Operated System for Microassembly," Proceedings of International Precision Assembly Seminar, Springer,Berlin, Heidelberg, February 14, 2010, pp. 13–20.

[9] Popa, D. O., and Stephanou, H. E., 2004, "Micro and Mesoscale Robotic Assembly," J. Manuf. Process., **6**(1), pp. 52–71.

[10] Popa, D. O., Murthy, R., and Das, A. N., 2009, "M3-Deterministic, Multiscale, Multirobot Platform for Microsystems Packaging: Design and Quasi-Static Precision Evaluation," IEEE Trans. Autom. Sci. Eng., **6**(2), pp. 345–361.

[11] Klotz, J. F., Wei, D., Yang, Z., Zhang, R., Sherehiy, A., Saadatzi, M. N., and Popa, D. O., 2019, "Concept Validation for a Novel Stick-and-Slip, Light-Powered, Mobile Micro-Crawler," Proceedings of International Conference on Manipulation, Automation and Robotics at Small Scales (MARSS), Helsinkl, Finland, July 1–5, pp. 1–7.

[12] Das, A. N., and Popa, D. O., 2011, "Precision Evaluation of Modular Multiscale Robots for Peg-in-Hole Microassembly Tasks," Proceedings of IEEE/RSJ International Conference on Intelligent Robots and Systems San Francisco, CA, Sept. 25–30, pp. 1699–1704.

[13] Pac, M. R., and Popa, D. O., 2011, "3-DOF Untethered Microrobot Powered by a Single Laser Beam Based on Differential Thermal Dynamics," Proceedings of IEEE International Conference on Robotics and Automation, Shanghai, China, May 9–13, pp. 121–127.

[14] Que, L., Park, J.-S., and Gianchandani, Y. B., 2001, "Bent-Beam Electrothermal actuators-Part I: Single Beam and Cascaded Devices," J. Microelectromech. Syst., **10**(2), pp. 247–254.

[15] Gauthier, M., and Régnier, S., 2011, *Robotic Microassembly*, Wiley, Hoboken, NJ.

[16] Koichi, H., and Tom, H., 1993, *Visual Servoing: Real-Time Control of Robot Manipulators Based on Visual Sensory Feedback*, World Scientific, Singapore.

[17] Hutchinson, S., Hager, G. D., and Corke, P. I., 1996, "A Tutorial on Visual Servo Control," IEEE Trans. Rob. Autom., **12**(5), pp. 651–670.

[18] Fang, Y., Dawson, D., Dixon, W., and Dequeiroz, M., 2002, "2.5 D Visual Servoing of Wheeled Mobile Robots," Proceedings of the IEEE Conference on Decision and Control, Las Vegas, NV, Dec. 10–13, pp. 2866–2871.

[19] Vikramaditya, B., and Nelson, B. J., 1997, "Visually Guided Microassembly Using Optical Microscopes and Active Vision Techniques," Proceedings of International Conference on Robotics and Automation, Albuquerque, NM, Apr. 20–25, pp. 3172–3177.

[20] Das, A. N., Zhang, P., Lee, W. H., Popa, D., and Stephanou, H., 2007, "μ 3: Multiscale, Deterministic Micro-Nano Assembly System for Construction of on-Wafer Microrobots," Proceedings of IEEE International Conference on Robotics and Automation, Roma, Italy, Apr. 10–14, pp. 461–466.

[21] Zhang, R., Wei, D., and Popa, D. O., 2018, "Design, Analysis and Fabrication of sAFAM, a 4 DoF Assembled Microrobot," Proceedings of International Conference on Manipulation, Automation and Robotics at Small Scales (MARSS), Nagoya, Japan, July 4–8, pp. 1–6.

[22] Zhang, R., Sherehiy, A., Yang, Z., Wei, D., Harnett, C. K., and Popa, D. O., 2019, "ChevBot–an Untethered Microrobot Powered by Laser for Microfactory Applications," Proceedings of International Conference on Robotics and Automation (ICRA), Montreal, QC, Canada, May 20–24, pp. 231–236.

Downloaded from http://asmedigitalcollection.asme.org/micronanomanufacturing/article-pdf/8/4/041011/6627640/jmnm_008_04_041011.pdf by a0sher02@louisville.edu on 15 March 2021